THE ASTROPHYSICAL JOURNAL, 567:412–422, 2002 March 1

INFRARED SPACE OBSERVATORY OBSERVATIONS OF THE UNIDENTIFIED 30 MICRON FEATURE IN PROTO–PLANETARY NEBULAE[1]

KEVIN VOLK AND SUN KWOK[2]
Department of Physics and Astronomy, University of Calgary, Calgary, AB T2N 1N4, Canada;volk@iras.ucalgary.ca, kwok@iras.ucalgary.ca
BRUCE J. HRIVNAK
Department of Physics and Astronomy, Valparaiso University, Valparaiso, IN 46383-6493; bruce.hrivnak@valpo.edu
AND
RYSZARD SZCZERBA
Nicolaus Copernicus Astronomical Center, Toruń, Laboratory for Astrophysics I, U1. Rabianska 8, 87-100 Torun, Poland; szczerba@ncac.torun.pl

Received 2001 July 18; accepted 2001 October 10

ABSTRACT

The intrinsic emission profile of the unidentified broad 30 μm emission feature is derived from *Infrared Space Observatory* (*ISO*) spectra of proto–planetary nebulae (PPNs). The feature is resolved into two components: a narrower feature at 26 μm and a broader feature at 33 μm. The intrinsic profiles of these two features and their varying strengths in PPNs are determined. The chemical origin of these features and the processes responsible for their changing strengths from asymptotic giant branch (AGB) stars to PPNs to planetary nebulae are discussed.

Subject headings: circumstellar matter — infrared: stars — ISM: lines and bands — planetary nebulae: general — radiative transfer — stars: AGB and post-AGB

1. INTRODUCTION

The unidentified broad emission feature around 30 μm was discovered by Forrest, Houck, & McCarthy (1981) from Kuiper Airborne Observatory observations. It was first seen in carbon-rich asymptotic giant branch (AGB) stars (IRC +10216 and AFGL 3068) and planetary nebulae (PN) IC 418 and NGC 6572. More recently, the 30 μm feature was found to be common in carbon-rich proto–planetary nebulae (PPNs), especially those showing the unidentified 21 μm emission feature (Omont et al. 1995; Szczerba et al. 1997, 1999).

The origin of the 30 μm feature is not known. The fact that a significant fraction of the total luminosity ($\sim$20% in PPNs; Hrivnak, Volk, & Kwok 2000) of the object is emitted in this feature suggests that the carrier must be composed of abundant elements. The first suggested identification was made by Goebel & Moseley (1985) who, on the basis of a comparison with laboratory measurements (Nuth et al. 1985), proposed that this feature is due to solid MgS, either as separate grains or as a surface coating. The alternative suggestion that the carrier is a carbonaceous material continues to be appealing because the feature is seen only in carbon-rich objects.

The *Infrared Space Observatory* (*ISO*) has excellent spectral coverage in the 30 μm region and for the first time offers the opportunity to derive a precise spectral signature of this feature. Substructure in the 30 μm feature has been recognized by Szczerba et al. (1999) and then resolved into two components called the "26 μm" and "30 μm" features in the *ISO* spectra of several PPNs (Hrivnak et al. 2000) and several carbon stars (Volk, Xiong, & Kwok 2000). Gaussian representations of these two features were used in the fittings of the *ISO* spectra of these PPNs (Hrivnak et al. 2000).

PPNs are objects in transition from the AGB to the PN phase (Kwok 1993). After mass loss has completely depleted the hydrogen envelope of an AGB star, the remnant circumstellar envelope continues to expand and disperse into the interstellar medium. While the circumstellar envelopes of many evolved AGB stars are optically thick in the infrared, they become optically thin as the result of continued expansion and geometric dilution as the object evolves beyond the AGB phase. Consequently, the dust envelopes of most PPNs are optically thin at 30 μm. Since the observed flux is directly proportional to emissivity under optically thin conditions, the infrared spectra of PPNs allow one to separate the contributions from different dust components and derive their opacities. PPNs also have the simplicity that their dust envelopes are completely heated by the photospheric radiation from the central stars. This is in contrast to PNs, in which the dust is heated by a combination of stellar photons, nebular line radiation (in particular Lyα), and collisions by free electrons. The radiation transfer problem is, therefore, not as complicated for PPNs as for PNs, and the observed spectra are more easily interpreted.

In this paper, we have derived empirical emissivities for the 26 and 30 μm features using the *ISO* spectra of several PPNs. From these, feature shapes and strengths have been derived. We have used a larger sample of 30 μm emission sources and included more *ISO* data at longer wavelengths than were used in the study of Hrivnak et al. (2000), and this has allowed us to improve on their preliminary results regarding the 30 μm source profiles and strengths.

[1] Based on observations made with *ISO*, an ESA project with instruments funded by the ESA member states (especially the PI countries: France, Germany, the Netherlands, and the United Kingdom) with the participation of ISAS and NASA.

[2] Canada Council Killam Fellow.

2. OBSERVATIONS

The infrared spectra of PPNs reported here were obtained with the *ISO* Short Wavelength Spectrometer (SWS), Long Wavelength Spectrometer (LWS), and Imaging Photopolarimeter and Spectrophotometer (ISOPHOT). The basic SWS observations were carried out in the SWS01 mode covering the spectral range 2.4–45 μm at scanning speeds 1 or 2, giving effective resolutions of $\lambda/\Delta\lambda \sim 250$. Five of the SWS observations were carried out in the higher resolution SWS06 mode between 23 and 43 μm with an effective resolution of $\sim$600, and six were carried out in the SWS06 mode between 16.5 and 24 μm with an effective resolution of $\sim$2000. The LWS observations were carried out in the LWS01 mode, covering the full spectral range of 43–195 μm at a resolution $\sim$200. The ISOPHOT observations were made in the spectrophotometer (PHT-S) mode in two wavelength ranges, 2.5–4.9 μm and 5.9–11.6 μm with resolutions of $\sim$80 and $\sim$90, respectively.

The PPNs chosen for this program are the eight for which good quality *ISO* data exist that cover the full SWS spectral range and that have strong 30 μm features. The data for these PPNs were extracted from the *ISO* archive, and the names of the original observing programs are listed in Table 1.

The reduction of the SWS data was carried out using version 9.5 of the standard pipeline processing. Once the autoanalysis results files had been obtained, they were further analyzed using the *ISO* Spectral Analysis Package (ISAP). After obviously bad data points were removed, the data were averaged with a uniform wavelength spacing in each section to produce the final spectra. More details of this reduction process are given by Hrivnak et al. (2000).

The LWS01 data were also reduced using version 9.5 of the standard pipeline processing. Further processing was carried out using ISAP version 2.1 and version 10 of the LWS calibration files. Each spectrum was first averaged to the default resolution of 0.0673 μm in each detector. The spectral sections were then defringed. Good agreement was found between detector 0, covering 43–52 μm, and detector 1, covering 49–64 μm. The final spectra were formed by averaging over the complete set of detectors, scaled to detector 1.

The PHT-S data were reduced using the PHOT Interactive Analysis (PIA) program version 7.3.2 at IPAC. Photometric calibration techniques are discussed by Schulz et al. (1999) and by Klaas et al. (2002). The standard processing procedure was used except for the photometric calibrations; the absolute calibration was carried out using dynamical calibration for the staring observations and using the special chopped-mode calibration for the chopped observations. More details of the reduction are given by Hrivnak et al. (2000).

3. COMBINING THE *ISO* DATA SETS

Three of the sources, IRAS Z02229+6208, IRAS 16594−4656, and IRAS 22272+5435, appear to have a strong peak at 26 μm based upon the *ISO* data (Hrivnak et al. 2000). However, there is some uncertainty in the strength of this feature. This is due to the discontinuous drop in the flux level in band 4 (29.5–45 μm) and the noisiness in the adjoining band 3E (27.5–29.5 μm) data. Hrivnak et al. (2000) choose to discount the band 3E data and assume that the large drop in band 4 was real. With these additional data, we can better investigate the correct flux levels. The spectra of these three sources will be discussed in detail below.

3.1. IRAS 22272+5435

Several sets of *ISO* data are available for this source, including SWS01, SWS06 (23–43 μm), SWS06 (16.5–24 μm), and LWS01. These data sets are plotted in Figure 1. The shorter wavelength (bands 1−3, 2.4–29.5 μm) and longer wavelength (band 4, 27.5–45 μm) bands of SWS01 and SWS06 have been distinguished by different colors. It can be seen that the flux levels of the different data sets differ from one another in their regions of overlap (Fig. 1*a*). However, in general they have very similar shapes. While the SWS06 (16.5–24 μm) observations in band 3 agree well with the SWS01 observations in that band, the SWS06 (23–43 μm) observations in band 3 are slightly higher when compared with the SWS06 (16.5–24 μm) observations. Most significantly, the SWS01 band 4 data are substantially lower than the SWS06 band 4 data as well as the LWS01 data.

In order to decide which data set have the correct absolute flux levels, we have compared them with the well-calibrated *IRAS* photometry. Synthetic *IRAS* fluxes for the SWS01, SWS06, and LWS01 data were computed using ISAP software. Since the long wavelength LWS region of the *ISO* spectra are likely to be contaminated by cirrus, and we do not have an off-source spectrum to correct for the cirrus contribution, we have instead added the expected cirrus component to the *IRAS* 100 μm flux using the cirrus-to-source ratio given in the *IRAS* Point Source Catalog (PSC). The *ISO* LWS01 data give simulated 60 and 100 μm *IRAS* fluxes of 100 and 48 Jy that agree with the actual observed *IRAS* PSC fluxes of 96.6 $\pm$ 9.7 and 46.3 $\pm$ 5.6 Jy. These comparisons suggest that the *ISO* LWS01 absolute fluxes are approximately correct.

TABLE 1

ISO OBSERVING PROGRAMS FOR THE SOURCE DATA

IRAS ID	SWS01	SWS06 (20 μm)	SWS06 (30 μm)	LWS01	PHT-S
Z02229+6208.....	bhrivnak.swsppn01	skwok.21micron	...	...	bhrivnak.swsppn02
07134+1005	kvolk.21micpro	skwok.21micadd	...	...	...
16594−4656	pgarcia.pne	...	...	pgarcia.pne	...
19500−1709	rwaters.postagb	...	rszczerb.30_um	mbarlow.dust3	rwaters.postagb
20000+3239	bhrrivnak.swsppn01	skwok.21micron	rszczerb.30_um	...	bhrivnak.swsppn02
22272+5435	proche.stardust	skwok.21micron	rszczerb.30_um	mbarlow.dust3	rwaters.postagb
22574+6609	bhrivnak.swsppn02	skwok.21micron	rszczerb.30_um	...	...
23304+6147	rwaters.postagb	skwok.21micron	rszczerb.30_um	...	...

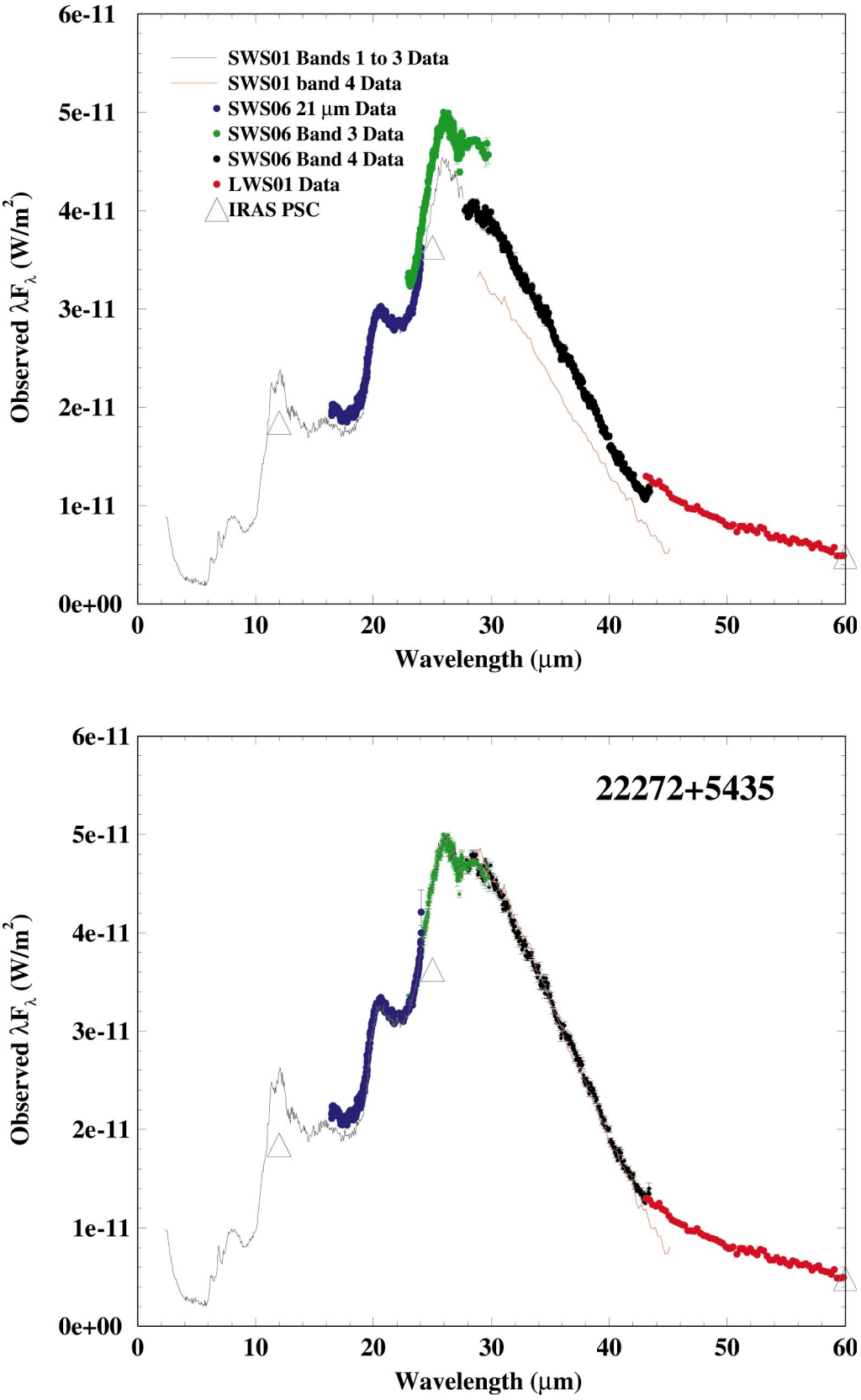

FIG. 1.—*Top*: *ISO* spectroscopic data for IRAS 22272+5435. Data plotted are SWS01 bands 1–3D (*black line*); SWS01 band 4 (*red line*); SWS06 (16.5–24 μm) observations (*blue circles with error bars*); SWS06 (23–43 μm) observations in band 3 (*green circles with error bars*); SWS06 (23–43 μm) observation in band 4 (*black circles with error bars*); and LWS01 (*red circles with error bars*). *IRAS* PSC points are shown as open triangles. *Bottom*: *ISO* spectroscopic data for IRAS 22272+5435 after scaling to produce agreement with *IRAS* photometry values (see text).

Similar comparisons with *IRAS* 12 and 25 μm PSC fluxes show that the SWS01 data are about 10% too low. The best agreement with the LWS01 spectrum in the overlap region and with the *IRAS* photometry is obtained if the other SWS spectra are scaled to agree with the band 3 SWS06 (23–43 μm) data. Thus, the SWS01 and SWS06 (16.5–23 μm) data were scaled up by a factor of 1.10; the band 4 SWS06 (27–43 μm) data were scaled up by a factor of 1.18; and the SWS01 band 4 (27–45 μm) data were scaled up by an additional factor of 1.31. This results in a smooth spectrum over all of the *ISO* data sets for IRAS 22272+5435 (see Fig. 1*b*). The simulated *IRAS* 12 and 25 μm fluxes calculated from this spectrum are 66 and 304 Jy compared to the actual observed fluxes of 73.9 ± 2.2 and 302.4 ± 9.1 Jy, respectively. While the 25 μm flux compares well, the simulated 12 μm flux is still too low by 11%. Although this could be attributed to calibration errors in the shorter wavelength parts of SWS01, we are unable to make simple corrections without jeopardizing the agreements in other parts of the spectrum. We will use this scaled, composite spectrum as the best available infrared spectrum of IRAS 22272+5435, realizing that there may be some uncertainty in the flux level on the shorter wavelength end.

3.2. IRAS 16594−4656

For this source, there are fewer data because no SWS06 observations were made; the only *ISO* observations available are the SWS01 and LWS01 spectra. The same discrepancy between the SWS01 band 3E and band 4 flux levels seen in IRAS 22272+5435 is also seen in IRAS 16594−4656. A flux jump at 29.5 μm in the spectrum of IRAS 16594−4656 was noted by Garcia-Lario et al. (1999). A comparison of the LWS01 and SWS01 band 4 observations show that the latter are about 10% lower in the overlap region. In turn, a comparison of the synthetic photometry from the *ISO* LWS01 spectrum with the *IRAS* 60 and 100 μm fluxes suggests that the LWS01 values are ∼10% too low. Scaling by a factor of 1.10, the LWS01 spectrum results in simulated *IRAS* 60 and 100 μm fluxes of 154 and 79 Jy, compared to actual observed fluxes of 131.4 ± 22.3 and 95.5 ± 14.3 Jy (after adjustment for cirrus contribution). In order to produce a smooth transition from SWS01 band 4 to LWS and to SWS01 band 3E, the SWS01 band 4 data were multiplied by a factor of 1.25.

With this scaling of band 4, the synthetic 12 and 25 μm fluxes are 42 and 343 Jy compared to the *IRAS* values of 44.9 ± 2.3 and 298.0 ± 14.9 Jy, respectively. These bracket the *IRAS* values, with the simulated 12 μm flux on the low side and the simulated 25 μm flux on the high side. This is not entirely satisfactory, but it does generally support the idea that the shorter wavelength parts of the SWS01 spectrum have about the correct flux level, whereas the band 4 section is too low. We also note that the SWS01 spectrum in bands 2 and 3 also agrees well with the *IRAS* Low Resolution Spectrometer data for this source.

3.3. IRAS Z02229+6208

For IRAS Z02229+6208, the only data sets are the SWS01 observations and the SWS06 (16.5–24 μm) observations. The SWS01 spectrum shows a sharp drop in the band 4 flux level relative to bands 3D and 3E, similar to that seen for IRAS 22272+5435. Without the LWS01 data, we cannot check the flux level at the long-wavelength end of SWS01 band 4. Multiplying the SWS01 band 4 data by a factor of 1.37 will produce a good agreement with band 3E. However, the simulated *IRAS* 25 μm flux is not sensitive to the level in band 4 since there is not much overlap between band 4 and the 25 μm *IRAS* filter profile, so scaling the band 4 data by 1.37 produces a change of less than 2% in the simulated *IRAS* 25 μm flux. Consequently, we cannot determine an independent confirmation of the correctness of this scaling using the observed *IRAS* flux. This source does have relatively good band 3E data because it is bright, so scaling the band 4 data to match band 3 should be reliable. We can therefore only conclude that the available data are consistent with the SWS01 band 4 data being low and in need of upward scaling.

3.4. *Problems with ISO SWS Band 4 Flux Levels*

From the above discussions, we concluded that there is a problem in the *ISO* SWS band 4 data for these three sources, with the fluxes being systematically too low. In a previous study (Hrivnak et al. 2000), we had assumed that the band 4 data were correct and that the band 3E data were not correct due to the fact that the band 3E data are usually of very poor quality with large uncertainties. We now believe that the band 3E data are probably correct in their flux levels and that the band 4 data have the right shape but are systematically low in flux. Thus, the detailed fittings and feature strengths for IRAS Z02229+6209 and IRAS 16594−4656 given by Hrivnak et al. (2000) are not correct (IRAS 22272+5435 was not included in that paper).

It is not clear to us what the cause of this loss of flux density in band 4 could be. If the sources were extended and filled the *ISO* apertures, one should see a progressive increase in the flux level from bands 3D to 3E to 4 due to the increase in aperture sizes. In fact, the band 3E data values are consistent with the band 3D data values, but the band 4 data values are lower. If this is due to a pointing problem, then the loss in flux should either be present in all the bands—as is seen in some *ISO* observations—or be worse in the shorter wavelength regions where the apertures are smaller.

For the other five PPNs studied, the differences between the band 3 and the band 4 data at the adjoining region are not large, so these band 4 data were not scaled. Also, for IRAS 19500−1709 there exist LWS01 data that bend smoothly with the SWS01 data where they join. Synthetic photometry of the observed, unscaled SWS01 and LWS01 spectra of IRAS 19500−1709 agrees very well with the observed *IRAS* fluxes. The simulated *IRAS* 60 and 100 fluxes are 75 and 19 Jy, as compared with the observed *IRAS* fluxes of 73.4 ± 8.8 and 18.6 ± 2.1 Jy (after cirrus adjustment), respectively.

4. DERIVATION OF THE EMISSION PROFILES

In order to derive the intrinsic properties of the features, one needs to first remove the continuum contribution. For these known carbon-rich objects, we assume the underlying continuum is due to amorphous carbon (AC) grains. Using the optical constants for Be1-AMC from Rouleau & Martin (1991) and the radiation transfer code of Leung (1976), the spectral energy distributions (SEDs) were fitted by one-dimensional radiation-transfer models. The dust envelope is assumed to be detached from the central star with an inner radius of r_0 and a density profile of $r^{-\alpha}$. A central star with a blackbody spectrum of temperature appropriate for its spectral type is assumed to be the sole heating source. More

TABLE 2

RESULTS OF MODEL FITS TO THE SEDs

IRAS ID	T_* (K)	α	L_*/D^2 ($L_\odot$ kpc^{-2})	$(\dot{M}/V)/D$ ($M_\odot$ yr^{-1}(km s^{-1} kpc)$^{-1}$)	r_{in}/D (10^{-3} pc kpc^{-1})
Z02229+6208.....	5500	2.5	1700	1.3×10^{-6}	3.4
07134+1005	7000	2.5	1400	7.2×10^{-7}	5.9
16594−4656	8000	2.5	1500	3.9×10^{-6}	5.5
19500−1709	8000	2.5	1400	1.3×10^{-6}	4.8
20000+3239	5500	2.5	630	5.1×10^{-7}	3.4
22272+5435	5500	2.5	2640	2.5×10^{-6}	5.6
22574+6609	5500	2.0	140	2.4×10^{-6}	0.87
23304+6147	5500	2.0	400	1.5×10^{-6}	4.3

details of this basic model and the SED fitting procedure are given by Hrivnak et al. (2000). A summary of the fitting parameters is listed in Table 2.

Two examples of the results of the fittings to the continuum are given in Figure 2 (IRAS 19500−1709) and Figure 3 (IRAS 23304+6147). In order to better define the SED and constrain the model, ground-based optical and near-infrared photometric measurements have also been included in the fittings. It is clear that several strong emission features are present above the continuum. The largest excess is in the form of a very broad ($\Delta\lambda \sim 16$ μm) feature seen around 30 μm (hereafter referred to as the "30 μm" feature), although narrower features can be seen at 8, 12, 20, and 26 μm. The 8 and 12 μm features have widths of $\sim$3 and $\sim$4 μm, respectively, and are likely to be due to bending modes of various side groups attached to aromatic rings (Kwok, Volk, & Bernath 2001). The 21 μm feature[3] ($\Delta\lambda \sim 2$ μm) has been extensively studied (Kwok, Volk, & Hrivnak 1989, 1999b; Volk, Kwok, & Hrivnak 1999) and has recently been suggested to be due to TiC clusters (von Helden et al. 2000) or oxygen-substitute five-member carbon rings (Papoular 2000).

[3] Although the peak wavelength of this feature is shown by Volk et al. (1999) to be at 20.1 μm, we will continue to call this the "21 μm" feature for historical reasons.

Figure 4 shows the spectrum of IRAS 19500−1709 after having been divided by the model continuum. The 30 μm feature is particularly strong in this source. Since the 21 μm and 26 μm features are weak compared to the 33 μm feature, this ratioed spectrum should be a good indicator of the intrinsic emission profile of the 33 μm feature.

The next best observations in this spectral region are the SWS01 and SWS06 observations of IRAS 23304+6147, the SWS01 and SWS06 observations of IRAS 20000+3239, and the SWS06 observations of IRAS 22272+5435. We have therefore used the continuum-divided spectra for these four sources as the primary data from which to derive the feature shapes. Secondary checks were made with the continuum-divided spectra of IRAS Z02229+6208 and IRAS 16594−4656, but they were given less weight due to the scaling applied to band 4. The other observations are of poorer quality. IRAS 22574+6609 is considerably fainter. Although IRAS 07134+1005 is one of the brighter sources, there were some problems with the observations, and both the SWS01 and SWS06 (23–43 μm) observations in band 4 turned out to be very noisy.

We proceeded to use the primary group of four sources to determine consistent profiles for the two features that we call the "26 μm" and "33 μm" features based upon their peak wavelengths. To display the emission features clearly, we ratioed each spectrum by the underlying continuum, fitting the continuum shape by a polynomial in different

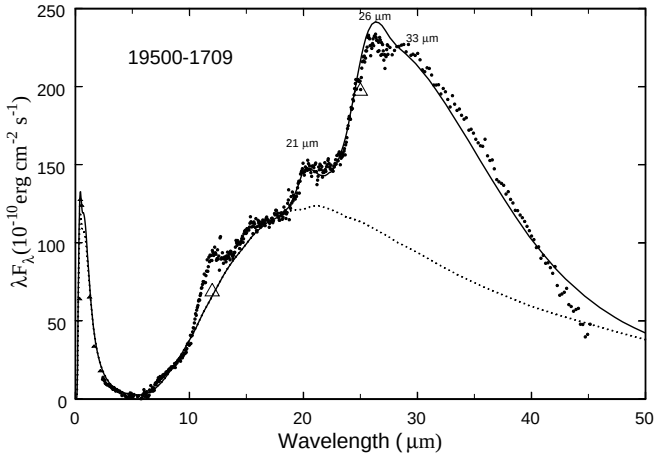

FIG. 2.—SED of IRAS 19500−1709, based upon *ISO* SWS01 data (*filled circles*), ground-based photometric (*filled triangles*), and *IRAS* PSC (*open triangle*) measurements. Also plotted are amorphous carbon continuum (*dotted line*) and the fit from the radiation transfer model, including derived 21, 26, and 33 μm features (*solid line*).

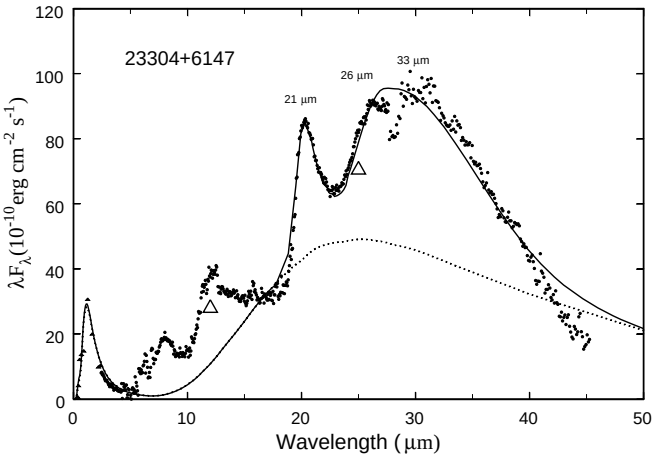

FIG. 3.—SED of IRAS 23304+6147 based upon *ISO* SWS01 data (*filled circles*), ground-based photometric (*filled triangles*), and *IRAS* PSC (*open triangles*) measurements. Also plotted are amorphous carbon continuum (*dotted line*) and the fit from the radiation transfer model, including derived 21, 26, and 33 μm features (*solid line*).

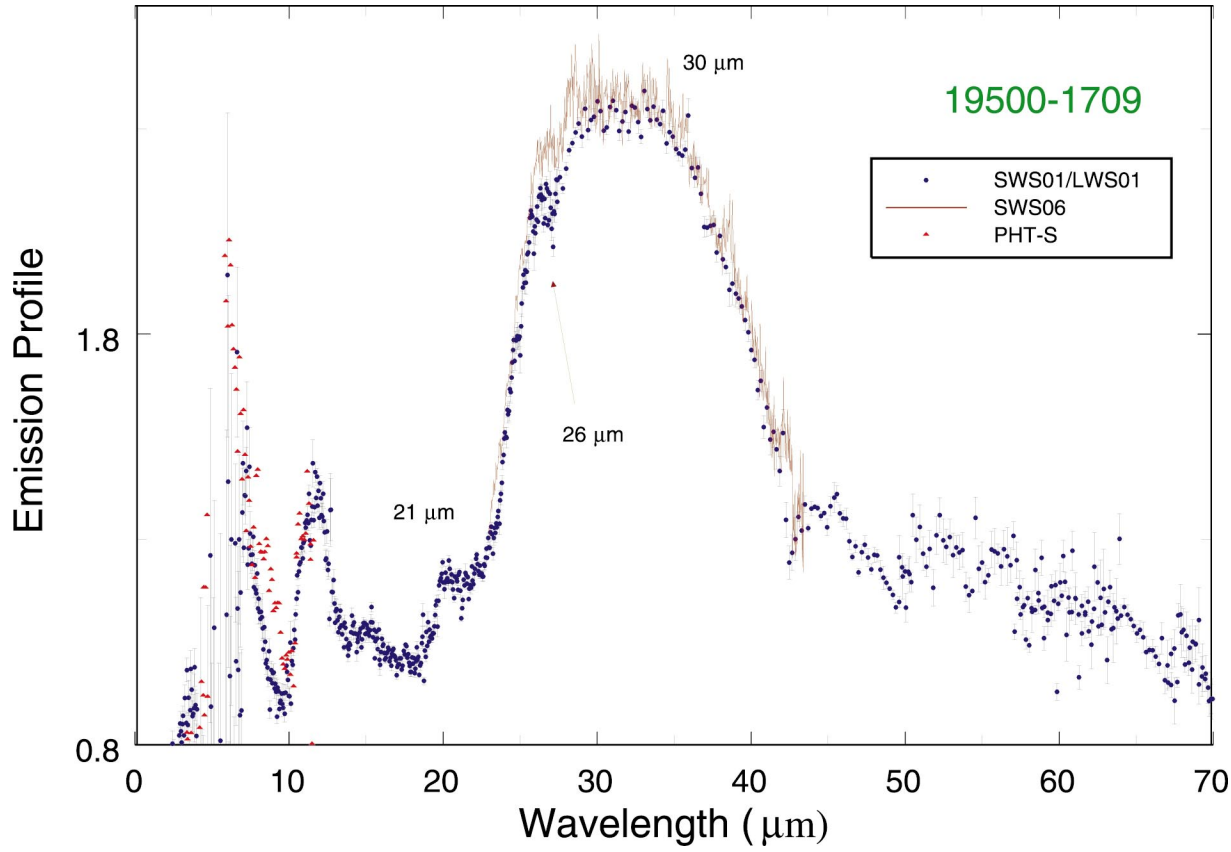

FIG. 4.—*ISO* SWS01 (*blue*), SWS06 (*brown*), LWS01 (*blue*), and PHT-S (*red*) spectra of IRAS 19500−1709 divided by model AC continuum

sections of the 19–44 μm range. The 26 μm feature is easily fit in general from the short wavelength edge to its peak at about 26.5 μm but becomes more uncertain from 27–32 μm, the region of significant overlap between the two components. Similarly, the longer wavelength part of the 33 μm feature is easily fit in general. In order to obtain a reasonable fit to these two features in the 27–33 μm wavelength range, we first assumed that the 26 μm feature is roughly symmetric about the peak and then adjusted its long-wavelength edge to produce a smooth shape for the 33 μm feature when the 26 μm feature was subtracted out. This required small adjustments to the 26 μm feature shape from 31–33 μm.

The long-wavelength section of the 33 μm feature, from 43–46 μm, is a linear extrapolation since the SWS06 observations do not extend beyond 43 μm. Similarly, we needed to carry out an extrapolation of the 26 μm feature profile to shorter wavelengths since the SWS06 (23–43 μm) observations start at 23 μm. When we carried out some trial fits to the full SWS06 data for the primary objects, including the 21 μm observations, we found that the 26 μm feature needed to have a short-wavelength wing so that the continuum level on either side of the 21 μm feature could be matched. A linear extrapolation of the profile was used, and the termination point was varied until a good fit to the combined SWS06 observations was obtained. This was found to successfully fit sources with widely different 21–26 μm feature strengths. Therefore, the flux levels around the 21 μm feature must scale with the 26 μm peak strength rather than being a separate component or being associated with the 8 and 12 μm plateau features.

The resulting profiles for the two components of the 30 μm feature are shown in Figure 5, normalized to peak values of 1.0. The peak of the shorter wavelength feature (26 μm feature) is 26.5 μm, and the feature FWHM is 5.85 μm. The other component (33 μm feature) peaks at 33.0 μm, with an uncertainty of ±0.5 μm arising from the dependence of the peak upon the shape assigned to the long wavelength wing of the 26 μm feature as it goes to zero. The

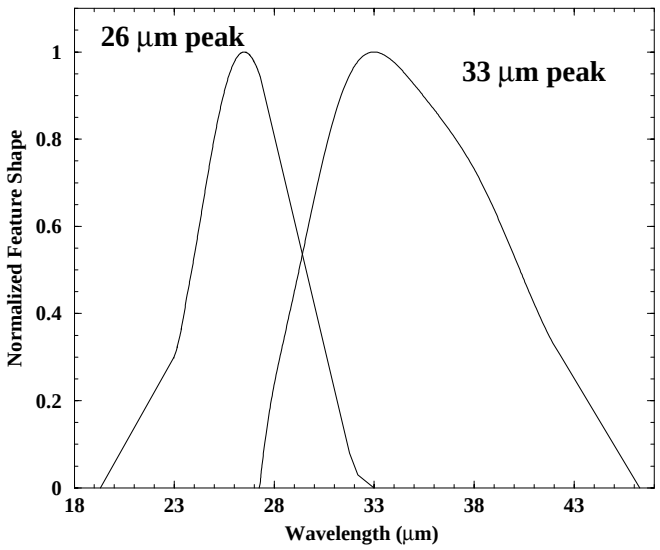

FIG. 5.—Normalized emission profiles of 26 and 33 μm features

TABLE 3

BASELINE FITTING COEFFICIENTS OF THE FEATURES

Object (Observation)	a_0	a_1	a_2	a_3	a_4
Z02229+6208	1.18253	−0.02431	0.00051	...	...
07134+1005	1.00552	...	...	...	...
16594−4656	−0.30526	0.12579	−0.00216	...	...
19500−1709	0.74927	0.01588	−0.00014	...	...
19500−1709 (SWS06).....	0.99441	...	...	...	...
20000+3239	1.30721	−0.01799	...	...	...
22272+5435	1.15944	−0.01312	...	...	...
22272+5435 (SWS06).....	1.23000	−0.04599	0.00462	−0.000262	6.227×10^{-7}
22574+6609	0.59484	0.01871	...	...	...
22574+6609 (SWS06).....	0.65432	0.02058	...	...	...
23304+6147	0.67257	0.02395	−0.00058	...	...

33 μm feature has an asymmetric shape, as is the case for the 21 μm feature and the silicate 10 μm feature.

5. DERIVATION OF THE FEATURE STRENGTHS

Having determined the emission profiles of the features, one is in a position to derive the feature strengths in each of the objects. Assuming that these features are due to different grain components, the feature strengths relative to the underlying continua can be obtained by performing χ^2 fittings to the profiles.

The fits were carried out with 5 features: the 21 μm feature for which the normalized profile was given by Volk et al. (1999), the 26 and 33 μm features, and also two feature plateaus: one for the 6.2/6.8/7.6 μm features and the associated underlying continuum (the 8 μm plateau), and one for the 11.3/12.0/12.8 μm features and their associated underlying continuum (the 12 μm plateau). The profiles used for these plateau features were obtained from the *ISO* SWS01 observations of IRAS 22272+5435, in which these two plateau features are relatively strong (Kwok et al. 2001). We began with the fitting of the SWS01 spectra that cover a larger wavelength interval and for which the continuum levels are better defined than for the SWS06 spectra.We found that after dividing the observed spectrum by the AC continuum, a slow-varying baseline still remains. This baseline is removed by subtracting a polynomial of the form $y = a_0 + a_1\lambda + a_2\lambda^2 + a_3\lambda^3 + a_4\lambda^4$, where y is the ratio of the observed spectrum to the AC model continuum.

These were fitted automatically, without any human intervention. The fitting program produces the "best" values for all the normalized feature strengths and the best values for the baseline. The coefficients (a_0, a_1, a_2, a_3, a_4) used in the baseline fitting equation are listed in Table 3. The feature strengths relative to the continua used in the fits are listed in Table 4.

In addition to fitting the SWS01 data, we also investigated the use of the SWS06 spectra to derive the feature strengths. While the SWS06 data have better spectral resolution and often better signal-to-noise ratio than the SWS01 data, they suffer from an inadequate baseline to perform the fitting. For IRAS 20000+3239 and IRAS 23304+6147 there were no significant differences between the SWS06 and the SWS01 spectra, so we did not attempt to fit these. However, we did fit the other three for which SWS06 spectra were available. In the case of IRAS 22574+6609, the underlying continuum is nearly flat, and we are able to obtain a good fit automatically. In the other two cases (IRAS 19500−1709 and IRAS 22272+5435), the fittings were done manually. We have listed the derived feature strengths from both SWS01 and SWS06 in Table 4. The comparison of these results is an indication of the uncertainties involved.

Results of the fits are given in Figure 6. In almost all cases, the observed spectra are well fitted by the model. The main exception is IRAS Z02229+6208, in which the 8 um plateau feature cannot be fitted by the standard profile; in fact, it appears that instead there is a feature at $\sim$6 μm. In this object, a narrow feature is seen at 6.9 μm, but the strong 7.7 μm and broad 8 μm features seen in the other objects are absent; instead, there is a weak plateau from 7.3–9.5 μm and a feature at 6.3 μm (Hrivnak et al. 2000). It is this 6.3 μm feature and an excess above the model continuum that combine to produce the emission excess seen at $\sim$6 μm. Such an excess is also seen in IRAS 20000+3239, but there it is not very noticeable because it is superimposed on the wing of the strong 8 μm plateau. The strength of the 8 μm plateau feature for IRAS Z02229+6208 in Figure 6 was set to 2.5 for comparison purposes. It is notable that the other plateau feature in this source is fitted quite nicely by the standard profile and shows no sign of any unusual properties. In a few cases, such as IRAS 20000+3239, the fit from 38–46 μm is not good. Without LWS01 data at the longer wavelengths, it is hard to accurately determine the baseline level. In other cases (e.g., IRAS 07134+1005), the discrep-

TABLE 4

DERIVED FEATURE STRENGTHS RELATIVE TO THEIR CONTINUA

Object (Observation)[a]	8 μm Plateau	12 μm Plateau	21 μm	26 μm	33 μm
Z02229+6208	2.45[b]	0.64	0.20	1.75	1.99
07134+1005	4.96	0.84	1.21	0.56	0.68
16594−4656	3.71	0.12	0.38	0.77	0.82
19500−1709	0.57	0.48	0.14	0.96	1.23
19500−1709 (SWS06)...	...	...	0.10	1.21	1.39
20000+3239	7.04	0.33	0.28	1.06	1.30
22272+5435	3.84	0.91	0.42	1.80	1.96
22272+5435 (SWS06)...	...	...	0.37	1.55	1.68
22574+6609	4.78	0.33	0.31	0.96	1.54
22574+6609 (SWS06)...	5.26	0.36	0.34	1.06	1.79
23304+6147	22.66	2.15	0.98	0.98	1.21

[a] The fits were to the *ISO* SWS01 spectra unless otherwise noted.

[b] Approximate value based on eye estimate. This feature could not be fitted by the standard profile because of its shifted wavelength.

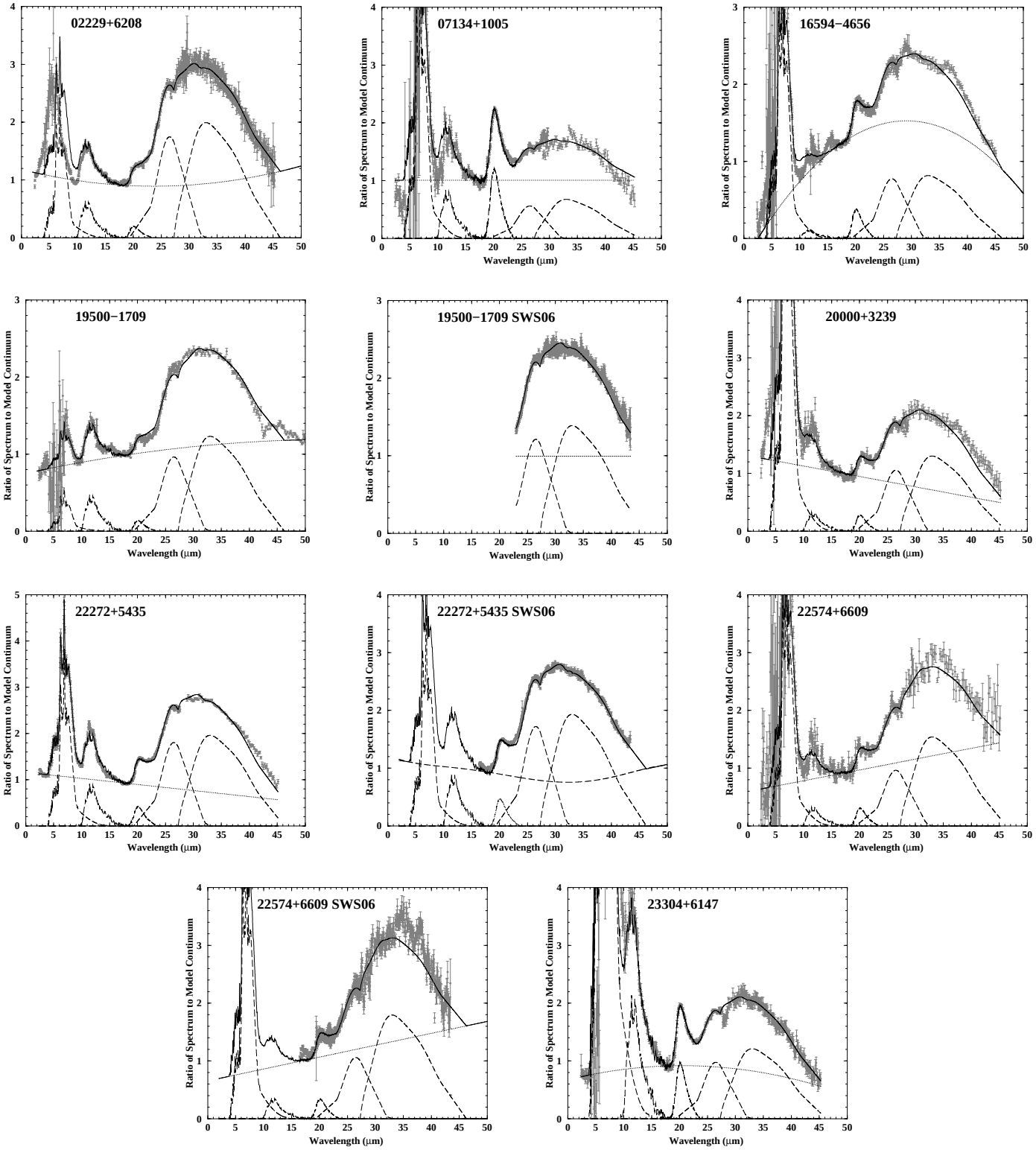

FIG. 6.—Model fits to ratioed spectra of IRAS Z02229+6208, 07134+1005, 16594−4656, 19500−1709, 20000+3239, 22272+5435, 22574+6609, and 23304+6147, showing contributions from each of the feature components. Dotted line represents polynomial fit to the slowly varying baseline.

ancy between the data and the fit is probably due to poor SWS01 band 4 data.

There are a few cases where there is a small bump in the ratio values at around 38 μm. This is seen in IRAS 16594−4656, IRAS 20000+3239, and possibly IRAS 22574+6609. This may be a real feature, but since a fair amount of manipulation of the band 4 data has been performed in order to remove the effects of glitches, it is not certain that the bump is real. It is not seen in the objects with the best-quality SWS06 observations.

Based upon the observed spectra (in some cases shifted in flux as described earlier) and the model fits, the percentage of the energy carried by each of the features has been determined. These are listed in Table 5. They represent the per-

TABLE 5

PERCENTAGES OF THE TOTAL FLUX EMITTED FROM EACH OF THE FEATURE COMPONENTS AND THE DUST CONTINUUM

IRAS ID	8 μm Plateau	12 μm Plateau	21 μm	26 μm	33 μm	Dust Continuum	Total of Features
02229+6208.....	7	6	1	15	13	58	42
07134+1005.....	5	6	7	7	7	68	32
16594−4656.....	5	1	2	7	7	76	23
19500−1709.....	1	4	1	12	12	71	29
20000+3239.....	8	3	2	13	12	62	38
22272+5435.....	6	7	3	15	15	54	46
22574+6609.....	12	4	1	10	7	64	35
23304+6147.....	9	9	5	12	12	52	48

centages of the flux from 2–1000 μm as derived from the model fits. Since the fits appear to be good, these values should be accurate to within a few percent of the total energy. There is a rather large range in the percentage of flux carried by a feature among the different PPNs. The plateau features vary over a very large range, with the first plateau varying from a high of 12% to a low of 1% and the second from 9% –1%. The 21 μm feature varies from a high of 7% in IRAS 07134+1005 and 5% in IRAS 16594−4656 to values as low as 1% in three of the sources. The range in the percentages of the 26 and 33 μm features is a factor of 2, from 7%–15% in each of these features. A correlation is seen between the percentage of the flux carried in the 26 and 33 μm features, with each of them carrying a similar percentage. This suggests a relationship between these two carriers, but one that does not include the 21 μm feature for which the percentage appears uncorrelated.

For some of the PPNs (i.e., IRAS 16594−4656), the percentages derived for the 21/26/33 μm features differ rather significantly from the values in Hrivnak et al. (2000). There are several reasons for this. For three of the objects, the band 4 flux has been scaled up to fit the rest of the spectrum (as described in §3), and this has increased the total infrared flux. With this has come changes in the continuum fitting. In cases such as IRAS Z02229+6208, where the continuum is displaced down a bit in the 15–35 μm region (compare Fig. 6 with Fig. 7 from Hrivnak et al. 2000), the features percentages have gone up. The opposite has happened in the case of IRAS 16594−4656.

6. DISCUSSION

6.1. *Origin of the* 26 *and* 33 μm *Features*

We begin by asking if the 26 and 33 μm features are related and if they have the same carrier. All eight of the PPNs in this study show both features, and as noted in the previous section, there appears to be a correlation in their strengths. Two additional PPNs were observed with *ISO* in this spectral region, and both also show both the 26 and 33 μm features in their spectra. They are IRAS 04296+3429 (Szczerba et al. 1999) and IRAS 22223+4327. We did not include them in this study, although they have SWS06 spectra, because they do not have SWS01 spectra from which to determine a reliable continuum. Thus, in all of the PPNs observed, both features are found together. They are also found together in the AGB star IRC +10216 and in the PNs IC 418 and NGC 7027. Since we find no evidence of only one of these features being found alone, we tentatively conclude that they either arise from the same carrier or from two closely related carriers.

The 26 and 33 μm features also coexist with the 21 μm feature and may be related. However, while all of the sources with the 21 μm feature also display the 26 and 33 μm features, the converse is not true; e.g., the 21 μm feature is not seen in all the PNs that show the 26 and 33 μm features.

Given the fact that the 26 and 33 μm features coexist with the aromatic infrared bands (AIBs) in PPNs, it is natural to suspect that these features are related. The effects of surface functional groups in aromatic compounds were first studied by Duley & Williams (1981). A recent study by Papoular (2000) suggests that the 33 μm feature is due to peripheral OH groups attached to aromatic clusters. Since the vibrational frequency of the C-O-H group is dependent on the displacement of the OH pair, the resulting emission profile can be quite broad. Similarly, the 26 μm feature can arise from carbon rings linked by oxygen bridges (Papoular 2000).

If these identifications are correct, then they have implications beyond the carriers of the 26 and 33 μm features. If indeed there is a relationship between the 26 and 33 μm features and the AIB features, then, for example, the AIB features could be due to large amorphous aromatic compounds rather than due to small, gas-phase polycyclic aromatic hydrocarbons (PAHs), as is commonly believed. The presence of aliphatic structures is already known in PPNs (Kwok et al. 1999a), making the suggestion of other functional groups plausible.

6.2. *Evolution of the* 30 μm *Feature from AGB Stars to PNs*

It is instructive to see how the 30 μm feature (26 μm + 33 μm) changes its appearance in the infrared spectra from extreme carbon stars to PPNs to PNs. This is illustrated in Figure 7. The left-hand side of the figure shows the observed spectra of the carbon star IRAS 21318+5631 (Volk, Xiong, & Kwok 2000), the PPN IRAS 16594−4656 (this paper), and the young PN NGC 7027. For comparison, the right-hand side of the figure shows the evolution of model spectra for both the AC dust continuum as well as the total emission, including the 21, 26, and 33 μm features. In the carbon star stage, the dust envelope is entirely optically thick (optical depth = 330 at V). The dust envelope is characterized by a color temperature of ∼200 K, with the AC continuum peaking at ∼15 μm. As mass loss stops and the dust envelope detaches from the central star, the optical depth drops to 5.3 in the PPN phase. Since the dust cools as it expands, the peak of the AC dust continuum is now at ∼20 μm. The 30 μm feature appears very prominent. When the star enters the PN stage, photoionization of the gaseous envelope leads to the creation of large numbers of recombination and collisionally excited lines. The dust cools to ∼150 K, and the spectrum peaks at ∼30 μm. Since the continuum peaks at the same wavelength as the 30 μm

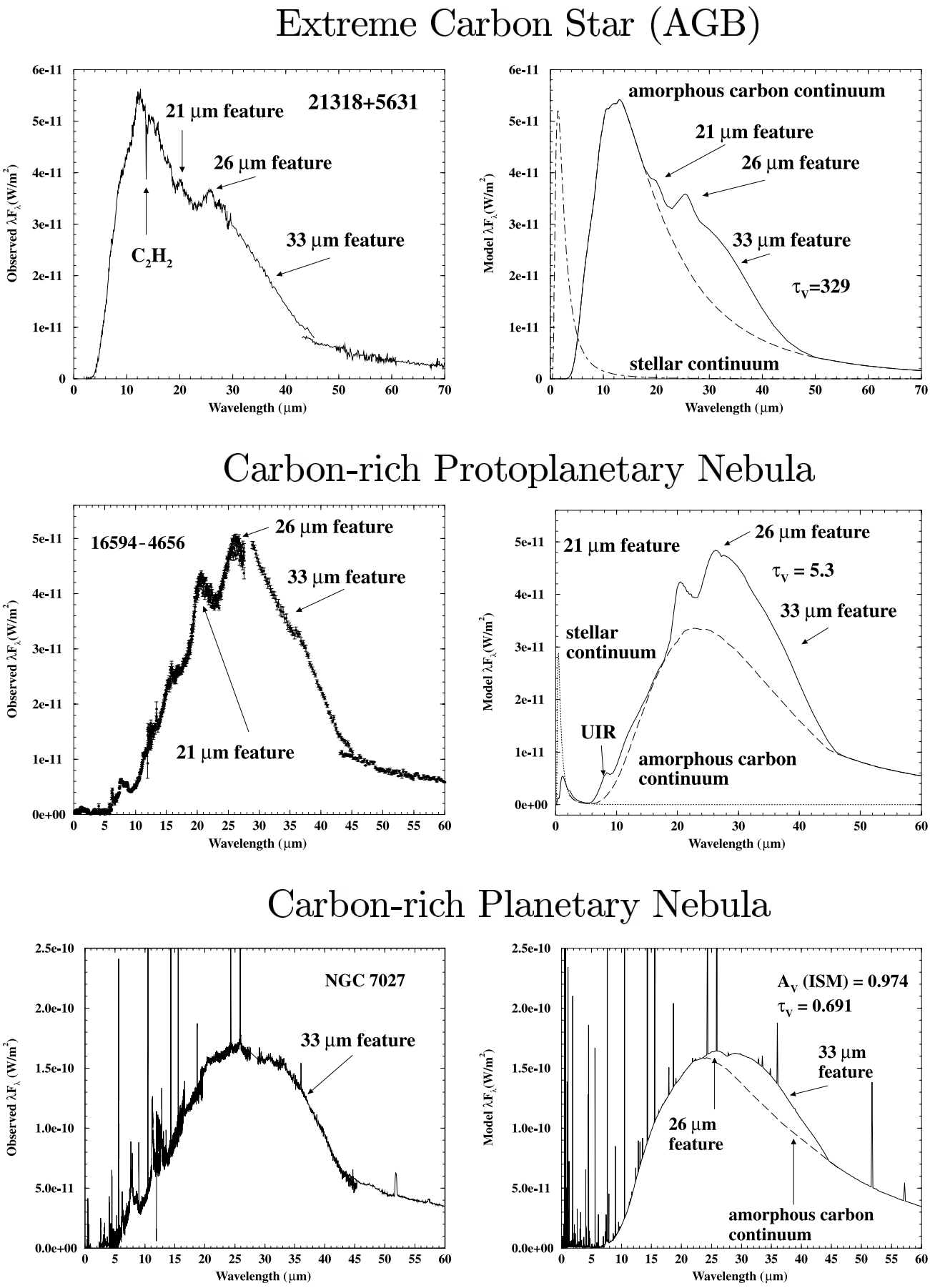

FIG. 7.—Evolution of infrared spectra from an extreme carbon star (*top*), through a PPN (*middle*), to a PN (*bottom*). Observed and model spectra are shown in left and right columns, respectively.

feature, it may become difficult to distinguish between the two. This is the reason why the 30 μm feature in NGC 7027 was not initially recognized (McCarthy, Forrest, & Houck 1978). However, it is clearly present in the *ISO* spectrum of NGC 7027, as can be seen in the bottom right panel of Figure 7.

The spectral evolution presented in Figure 7 suggests that the observed strengths of the 21, 26, and 33 μm features vary with time as the star evolves from the AGB. If this is so, then the observed 30 μm feature strength could be used as an age indicator. However, such a method supposes that all stars begin with an equal abundance of the carrier, while we know that the abundance of the carrier is dependent on the elemental abundance of carbon.

Assuming that the feature strength does vary with time, what is the cause of variation? It may be a combination of the synthesis/destruction of the material and/or effects of excitation. In the AGB phase, the optical photons of the central star are all absorbed by the AC dust component, and the background radiation is made up of reradiated infrared photons. In the PPN phase, the dust envelope is no longer optically thick, and the star has evolved to an intermediate temperature. The majority of the background radiation is therefore visible starlight, and the resulting larger absorption cross section of the material will lead to a more prominent feature. In the PN phase, the star radiates primarily in the ultraviolet, and the visible background is made up of weak nebular continuum (bound-free and free-free) radiations. The lack of visible light could be responsible for the weakening of the 30 μm feature. Alternatively, there could be a real change in the abundance of the carrier. It is now known that complex organic molecular species exist in the circumstellar environment of post-AGB stars, and the nature of the carbonaceous compounds changes from aliphatic to aromatic during the evolution from the PPN to the PN phase (Kwok et al. 1999a). It is conceivable that the chemical structure of the 30 μm feature carrier undergoes significant changes over the same period. The 21 μm feature, for example, is observed only in PPNs and weakly in extreme carbon stars, suggesting that the carrier is destroyed before the star reaches the PN phase. Similarly, some destruction mechanism, such as the onset of fast outflows, could also affect the 30 μm feature carrier.

7. CONCLUSIONS

Based on the *ISO* spectra of PPNs, the intrinsic emission profile (and, therefore, the opacity) of the broad unidentified emission feature at 30 μm has been determined. By including more spectra with the 30 μm feature and by using *ISO* SWS06 and LWS01 data, we were able to improve upon the previous results of Hrivnak et al. (2000). We found that this feature can be resolved into a broad feature at 33 μm and a narrower feature at 26 μm. The broadness of the profiles suggests that they originate from a solid-state material, possibly arising from vibrational modes of a variety of functional groups attached to aromatic rings. Unfortunately, there has been very little laboratory work done at such long wavelengths. With the intrinsic profiles determined in the present work, it is hoped that this will motivate further laboratory spectroscopic studies, particularly of carbonaceous materials, in order to obtain a firm identification of the carriers of the 26 and 33 μm features.

K. V. and S. K. acknowledge support by the Natural Sciences and Engineering Research Council of Canada. B. J. H. acknowledges the support of NASA through contract 961534 from the Jet Propulsion Laboratory, and R. S. acknowledges the support by grant 2.P03D.020.17 from the Polish Committee for Scientific Research.

REFERENCES

Duley, W. W., & Williams, D. A. 1981, MNRAS, 196, 269
Forrest, W. J., Houck, J. R., & McCarthy, J. F. 1981, ApJ, 248, 195
Garcia-Lario, P., Manchado, A., Ulla, A., & Manteiga, M. 1999, ApJ, 513, 941
Goebel, J. H., & Moseley, S. H. 1985, ApJ, 290, L35
Hrivnak, B. J., Volk, K., & Kwok, S. 2000, ApJ, 535, 275
Klaas, U., Laureijs, R. J., Schulz, B., Acosta-Pulido, J. A., Abraham, P., & Lemke, D. 2002, The Calibration Legacy of the ISO Mission, ed. L. Metcalfe, & M. F. K. Kessler (ESA SP-481; Noordwijk: ESA), in press
Kwok, S. 1993, ARA&A, 31, 63
Kwok, S., Volk, K., & Bernath, P. 2001, ApJ, 554, L87
Kwok, S., Volk, K. M., & Hrivnak, B. J. 1989, ApJ, 345, L51
———. 1999a, A&A, 350, L35
———. 1999b, in IAU Symp. 191, Asymptotic Giant Branch Stars, ed. T. Le Bertre, A. Lébre, & C. Waelkens (San Francisco: ASP), 297
Leung, C. M. 1976, ApJ, 209, 75
McCarthy, J. F., Forrest, W. J., & Houck, J. R. 1978, ApJ, 224, 109
Nuth, J. A., Moseley, S. H., Silverberg, R. F., Goebel, J. H., & Moore, W. J. 1985, ApJ, 290, L41
Omont, A., et al. 1995, ApJ, 454, 819
Papoular, R. 2000, A&A, 362, L9
Rouleau, F., & Martin, P. G. 1991, ApJ, 377, 526
Schulz, B., Huth, S., Kinkel, U., et al. 1999, in The Universe as Seen by *ISO*, ed. P. Cox & M. F. Kessler (ESA-SP 427; Noordwijk: ESA), 89
Szczerba, R., Henning, Th., Volk, K., Kwok, S., & Cox, P. 1999, A&A, 345, L39
Szczerba, R., Omont, A., Volk, K., & Kwok, S. 1997, A&A, 317, 859
Volk, K., Kwok, S., & Hrivnak, B. J. 1999, ApJ, 516, L99
Volk, K., Xiong, G. Z., & Kwok, S. 2000, ApJ, 530, 408
von Helden, G., et al. 2000, Science, 288, 313